

RESEARCH ARTICLE

10.1002/2016JA022362

Reconnection layer bounded by switch-off shocks: Dayside magnetopause crossing by THEMIS D

Bengt Sonnerup¹, Götz Paschmann², Stein Haaland^{3,4}, Tai Phan⁵, and Stefan Eriksson⁶

Key Points:

- Unique magnetopause reconnection event, containing Alfvénic plasma jet wedged between switch-off shocks, has been discovered and analyzed
- MHD shock jump conditions account well for density, pressure, temperature, and entropy changes, and their dependence on the plasma beta
- Switch-off condition reveals the presence of heavy ions in the event and allows determination of the effective ion mass

Correspondence to:

B. Sonnerup,
Bengt.U.O.Sonnerup@dartmouth.edu

Citation:

Sonnerup, B., G. Paschmann, S. Haaland, T. Phan, and S. Eriksson (2016), Reconnection layer bounded by switch-off shocks: Dayside magnetopause crossing by THEMIS D, *J. Geophys. Res. Space Physics*, 121, 3310–3332, doi:10.1002/2016JA022362.

Received 12 JAN 2016

Accepted 5 APR 2016

Accepted article online 11 APR 2016

Published online 30 APR 2016

¹Thayer School of Engineering, Dartmouth College, Hanover, New Hampshire, USA, ²Max-Planck-Institut für extraterrestrische Physik, Garching, Germany, ³Max-Planck-Institut für Sonnensystemforschung, Göttingen, Germany, ⁴Birkeland Centre for Space Science, University of Bergen, Bergen, Norway, ⁵Space Science Laboratory, University of California, Berkeley, California, USA, ⁶Laboratory for Atmospheric and Space Physics, University of Colorado Boulder, Boulder, Colorado, USA

Abstract We discuss observations of reconnection, obtained by Time History of Events and Macroscale Interactions during Substorms (THEMIS) D during an outward bound traversal of the low-latitude dayside magnetopause. The reconnection signatures include high magnetic shear, a southward directed Alfvénic jet, bounded by slow-mode shocks near the switch-off limit (as in the symmetric Petschek geometry), a small, sunward directed normal magnetic field and plasma inflow into the jet from both sides. We conclude that cold, unmeasured ionospheric ions helped establish the symmetry. The effective ion mass, estimated from the switch-off condition, was 2.39 amu on the magnetospheric side, where the number density was inferred from the spacecraft potential, and 1.09 amu on the magnetosheath side. After a modest pressure correction in the magnetospheric shock, the MHD jump conditions for density, pressure, temperature, and entropy were well satisfied. The shock jumps were much larger on the magnetosphere side than on the magnetosheath side; we show this to be a plasma β effect. The main dissipation mechanism appears to be irreversible transfer between thermal motion parallel and perpendicular to the field, such that both shocks bring about approximate downstream temperature isotropy. Hall currents and electric fields were present, albeit in a strongly asymmetric configuration. The magnetospheric shock had longer duration than the magnetosheath one, possibly as a result of a nonconstant magnetopause speed. We infer an average earthward magnetopause speed (14 km/s), corresponding nominal shock thicknesses (12 and 6 λ_i), dimensionless reconnection rates (0.061–0.085), and reconnection wedge angles (5° between shocks; 13° between separatrices).

1. Introduction

Spacecraft observations of the magnetopause during reconnection events [e.g., Sonnerup *et al.*, 1995; Paschmann *et al.*, 2013, and references therein] have commonly, and with varying levels of success, been interpreted as crossings of a rotational discontinuity (RD). In this RD, the flow is Alfvénic and the directions of the tangential magnetic field and flow change from their magnetosheath to their magnetospheric orientations. This interpretation has its roots in the Levy *et al.* [1964] magnetopause reconnection model, in which the plasma pressure in the magnetosphere was assumed to be vanishingly small. This state is reached as the plasma from the magnetosheath flows across a slow-mode expansion fan, located earthward of the RD. In this fan, the plasma pressure and density drop to zero, and the field magnitude increases from its magnetosheath to its magnetospheric level.

For finite magnetospheric plasma density, there will usually be inflow into the magnetopause reconnection layer from both its magnetosheath and its magnetosphere side. On each side, the magnetopause structure then consists of intermediate and slow-mode standing waves [Petschek and Thorne, 1967; Lin and Lee, 1993]. If the plasma conditions and field strength on the two sides become comparable, the reconnection configuration can approach the symmetrical geometry described by Petschek [1964]. In this model, illustrated in Figure 1, the reconnection geometry is dominated by two slow-mode shocks near the switch-off limit, bounding wedge-shaped reconnection jets. The jets contain a weak normal field and compressed plasma, which has been accelerated in the shocks to approximately the upstream Alfvén speed, in the direction along the magnetopause, and away from the reconnection site. The symmetric configuration is applicable to reconnection

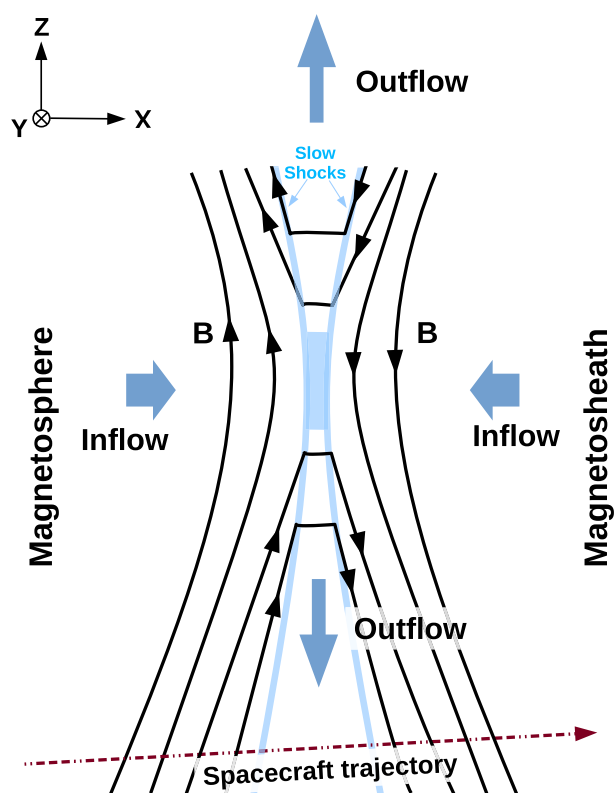


Figure 1. Schematic of the *Petschek* [1964] model, showing outflow jets bounded by two slow-mode shocks, with inflow from both sides. Wedge angle between the shocks is exaggerated.

in the geomagnetic tail, and also in some solar wind [Gosling *et al.*, 2005] events, and magnetosheath [Phan *et al.*, 2007] events. Slow shocks in the magnetotail have been analyzed in detail [e.g., Feldman *et al.*, 1985; Eriksson *et al.*, 2004]. In the present paper, we demonstrate that, under the right conditions, a similar reconnection geometry, albeit with important remaining asymmetric features, can occur at the magnetopause. One such nearly symmetric event was observed by the Polar spacecraft on 1 April 2001 [Mozer *et al.*, 2002]. In that crossing, the Hall magnetic and electric fields were observed and interpreted as evidence for encountering the ion diffusion region, which surrounds the magnetic X point. Our event occurs well away from the diffusion region, as illustrated by the spacecraft path in Figure 1. It still shows some magnetic and electric features believed to be driven by the Hall effects in the distant diffusion region, but now the slow-mode shocks are present as well and form a focus of our study.

The main purpose of our paper is to discuss, and quantitatively analyze, a crossing by Time History of Events and Macroscale Interactions during Substorms (THEMIS) D (ThD) of the dayside magnetopause at low southern GSM latitude. The event occurred on 3 August 2008, around 17:00 UT. This crossing shows signatures consistent with Figure 1, namely, high magnetic shear, a pronounced, southward directed, reconnection jet, inflow into this jet from both sides, near switch-off of the field components tangential to the magnetopause, and a small, sunward pointing, normal magnetic field. It is included as event 42 in the studies of electron and ion heating in reconnection exhausts by Phan *et al.* [2013, 2014].

Our presentation is organized as follows. In section 2, we present an overview of the event and discuss its various features. In section 3, we analyze the jump conditions, using a simple MHD model, and in section 4, we examine the various dissipation mechanisms. Finally, in section 5 we provide further discussion and a summary of our conclusions. The presence of unmeasured cold plasma is discussed in Appendix A.

A more detailed analysis of the jump conditions, which includes the effects of pressure anisotropy, along with a study of the behavior of the Chew-Goldberger-Low (CGL) double-adiabatic invariants, will be presented separately.

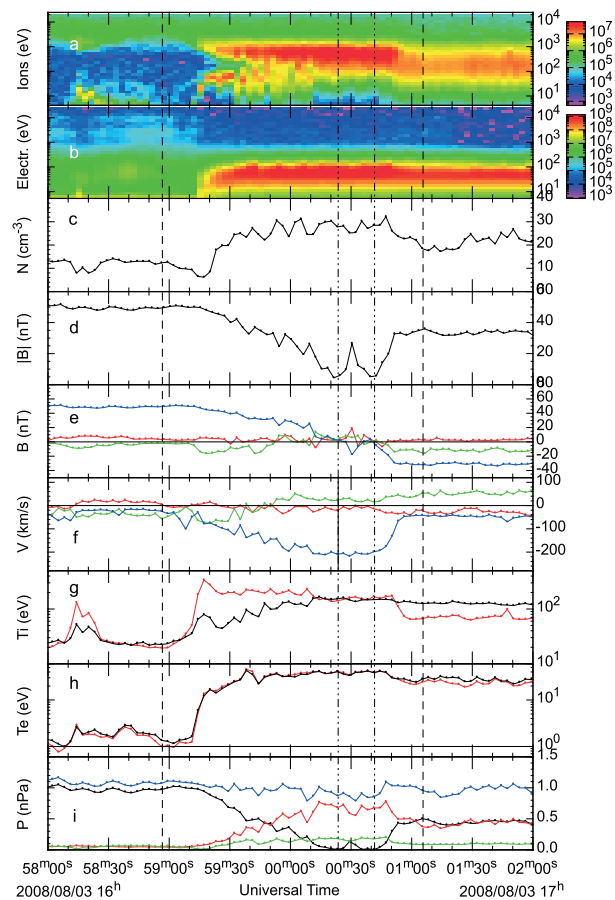


Figure 2. Overview of the 3 August 2008 magnetopause crossing by the ThD spacecraft, based on 3 s resolution plasma and magnetic field data: (a, b) ion and electron energy-time spectrograms (color bar units are eV/cm² s); (c) plasma number density (see Appendix A); (d) magnetic field magnitude; (e, f) components of the magnetic field and the plasma bulk velocity; (g) ion temperatures (red: T_{\parallel} , black: T_{\perp}); (h) same for electrons; (i) magnetic pressures (black), ion (red) and electron (green) perpendicular pressures, and sum of the pressures (blue). Vector quantities are in MVA coordinates, with x (red), y (green), and z (blue) along the minimum, intermediate, and maximum variance directions. Vertical lines mark the upstream (dashed) and downstream (dash dotted) reference times for the two shocks.

2. Observations

2.1. Overview

The 3 August 2008 event is an outbound crossing of the magnetopause by ThD at $X = 10.0$, $Y = 2.1$, and $Z = -3.8 R_E$, in GSM coordinates. Figure 2 shows the plasma and magnetic field data, based on 3 s resolution measurements by the electrostatic analyzer (ESA) [McFadden et al., 2008] and fluxgate magnetometer (FGM) [Auster et al., 2008] instruments. Vector quantities are shown in minimum-variance (MVA) coordinates (see section 2.2). The inner edge of the magnetopause is encountered near 16:59:00 UT, with exit into the magnetosheath near 17:01:00 UT. Substantial particle fluxes are first seen at about 16:59:15 UT (Figures 2a and 2b).

Figure 2c shows a net increase in plasma number density of ≈ 1.5 from the magnetosphere to the magnetosheath, making the boundary conditions more symmetric than is typical for the magnetopause. Note that the number density within the MP exhaust itself is enhanced by a factor of ≈ 1.5 over its magnetosheath value. The magnetosphere number density is around 12 1/cm³. As discussed in Appendix A, this value has been inferred from measurements of the spacecraft potential and is attributed to plasma below the energy range of the ESA ion instrument. When entering the exhaust jet, the cold plasma is accelerated and becomes visible to the instrument, as is apparent from the ion spectrogram in the top panel (after 16:59:15 UT). The plasma coming from the magnetosphere must also have contained heavier ions (see section 3.2).

The magnetic field transition from the magnetosphere to the magnetosheath (Figures 2d and 2e) is characterized by a change from a strongly northward to a strongly southward direction, a shear angle of about 152° , and a net drop in field magnitude by a factor of ≈ 1.4 , from 49.4 to 35.5 nT, with two deep minima (5.1 and 2.7 nT) in between. These minima are separated by a substantial field peak at 17:00:30 UT.

A strong, southward directed, plasma jet is present in the exhaust (Figure 2f), indicating that the crossing was located south of an active reconnection site. Consistent with this location, the normal magnetic field (Figure 2e) is on average pointing outward from Earth, $B_x > 0$. Comparison of the velocity component traces (Figure 2f) with the corresponding magnetic field component traces (Figure 2e) makes clear that when proceeding outward through the magnetopause, the velocity and magnetic field components are first correlated (in the interval between the times marked by the first pair of vertical lines) but then become anticorrelated (in the interval marked by the second pair). Combined with the outward directed B_x , this switch from correlation to anticorrelation means that there is inflow into the exhaust from both sides.

Figure 2g shows that the ion temperatures, particularly T_{\parallel} , strongly rise when entering the exhaust from the magnetosphere side. When entering from the magnetosheath side, there is only a small rise in T_{\perp} , but a more substantial rise in T_{\parallel} . The electrons (Figure 2h) show similar rises in temperature, but they are nearly isotropic. As explained in Appendix A, the temperatures are affected by the cold plasma on the magnetospheric side. Finally, Figure 2i shows that the magnetic and plasma pressures vary strongly, but their sum, i.e., the total pressure, is approximately, albeit not perfectly, preserved.

We will refer to the transitions on the magnetosphere and the magnetosheath sides as Shock 1 and Shock 2, respectively, in anticipation of their interpretation as near switch-off shocks. Such shocks are the strongest version of the slow-mode MHD shock. As the plasma moves across a slow-mode shock, the plasma density, temperature, and entropy, all increase, while the tangential field component decreases; in the switch-off version, the upstream normal flow component is Alfvénic, and the downstream tangential field component is reduced to zero.

2.2. Minimum Variance Analysis of the Magnetic Field

Minimum variance analysis (MVA) of the 0.25 s resolution magnetic field data for the entire magnetopause crossing (between the first and last vertical lines in Figure 2) yields an eigenvector belonging to the minimum eigenvalue, and interpreted as the boundary normal, of (0.9904, -0.0264 , -0.1358) in GSM, with an intermediate-to-minimum eigenvalue ratio of 5.3. This rather low value indicates a substantial uncertainty of the normal vector, mostly under rotations about the maximum variance axis (approximately the GSM z axis). The hodogram projections in Figure 3a illustrate the behavior of the 0.25 s field vectors; those in Figure 3b are based on the 3 s resolution spin-averaged field data for the same interval. For a description of the MVA technique, see *Sonnerup and Scheible* [1998]. The vector quantities in Figure 2 and subsequent figures have all been rotated into the MVA coordinates obtained from the high-resolution data.

As the hodograms at the top in each panel show, the magnetic field decreases its magnitude as the spacecraft crosses Shock 1, from the magnetosphere (top end of the upper hodograms) into the jet, and is nearly switched off before it grows again in approximately the opposite direction (more precisely, this direction is given by the 152° shear angle), as the spacecraft traverses Shock 2, into the magnetosheath (bottom end of the upper hodograms). The hodograms on the top right in each panel show that during this transition the minimum variance component, interpreted as the normal magnetic field component, although noisy, remains positive on average, +3.0 nT for the MVA in the top panel, and +2.7 nT for the MVA in the bottom panel. That a large majority of samples has a positive normal component is more clearly evident from the hodograms on the lower left in each panel. Overall, the field fluctuations are substantial at both time resolutions.

Since the exhaust is expected to be approximately wedge shaped, we also performed MVA for the two shocks separately but found Shock 2 to give an unacceptably low eigenvalue ratio, λ_2/λ_1 .

2.3. DeHoffmann-Teller Frame

The deHoffmann-Teller (HT) transformation velocity was obtained from the usual procedure of minimizing the electric field in the moving (HT) frame [*Khrabrov and Sonnerup*, 1998]. The correlation coefficient between the components of the computed convection electric field, $\mathbf{E}_C = -\mathbf{V} \times \mathbf{B}$, and the corresponding components of the HT electric field, $\mathbf{E}_{HT} = -\mathbf{V}_{HT} \times \mathbf{B}$, was 0.94. This value is not high, indicating that at least in some portions of the event, there were substantial deviations from steady, field-aligned flow (as seen in the HT frame).

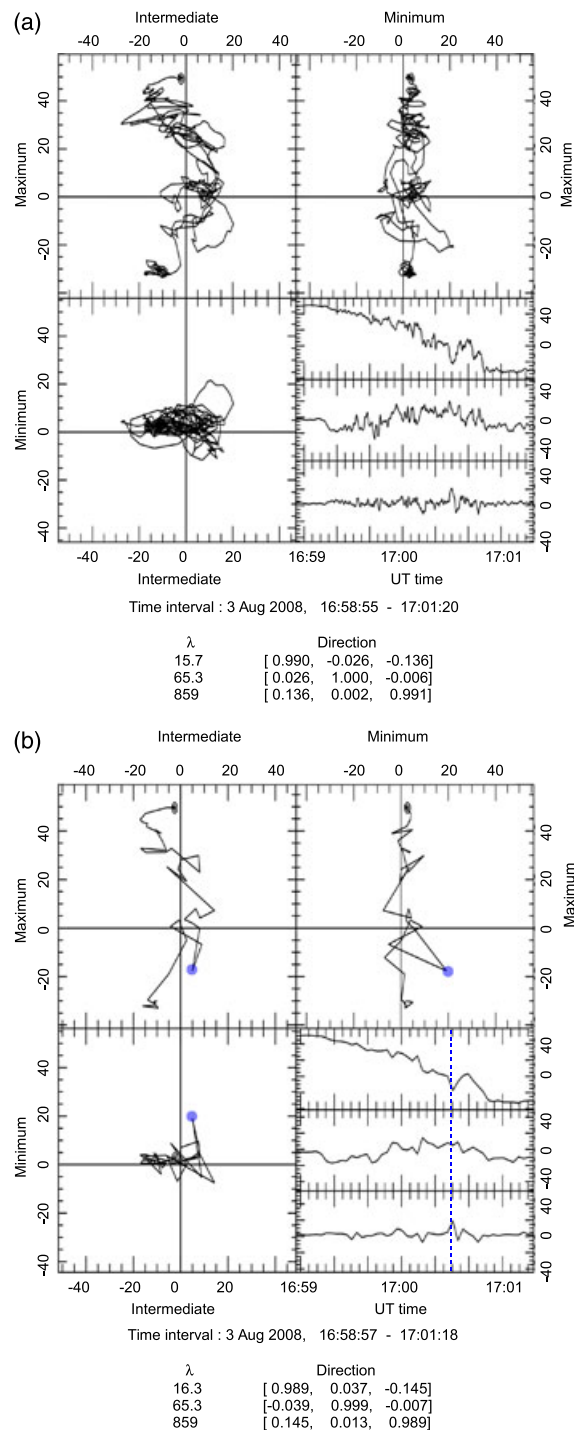


Figure 3. Magnetic field hodograms. (a) MVA of the 0.25 s resolution FGM data for the complete magnetopause layer. (top left) The progression of the magnetic field vector in the maximum-intermediate eigenvector plane (the plane tangential to the magnetopause), (top right) the progression in the maximum-minimum eigenvector plane, (bottom left) the projection in the minimum-intermediate plane, and (bottom right) the time series for the field components in the (top) maximum, (middle) intermediate, and (bottom) minimum variance directions. The magnetic field unit along the axes is nanotesla (nT). The table below the hodograms lists eigenvalues λ (in nT^2) and eigenvectors (in GSM). The eigenvector for the minimum eigenvalue (15.7 nT^2), interpreted as the boundary normal, is (0.9904, -0.0264 , -0.1358), with an intermediate-to-minimum eigenvalue ratio of 5.3. The magnetospheric ends are at the top in the two upper hodograms. (b) MVA of the spin-averaged (3 s resolution) magnetic field for closely the same interval, with a minimum eigenvalue of 16.3 nT^2 and an intermediate-to-minimum eigenvalue ratio of 4.0. In these low-resolution hodograms, the field maximum at 17:00:30 UT is marked by a blue dot.

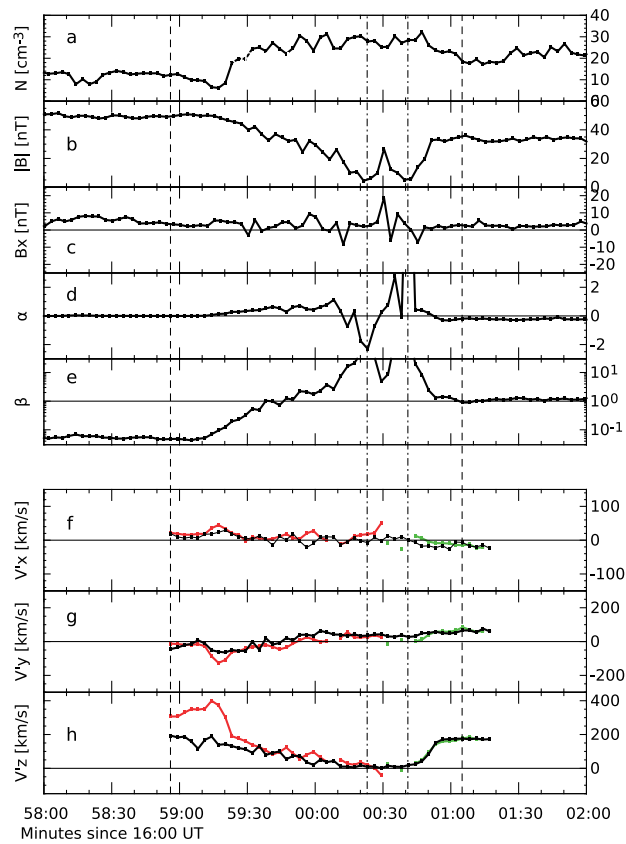


Figure 4. Walén test. Panel block on top shows relevant field and plasma information: (a) composite plasma number density; (b) magnetic field magnitude; (c) normal magnetic field B_x ; (d) combined pressure anisotropy factor $\alpha = (p_{\parallel} - p_{\perp})\mu_0/B^2$; (e) combined plasma $\beta = p 2\mu_0/B^2$, with $p = (2p_{\perp} + p_{\parallel})/3$. Panel block on bottom shows the Walén test: (f–h) the three components of $\mathbf{V}' \equiv (\mathbf{V} - \mathbf{V}_{HT})$ in black, overplotted on the corresponding components of \mathbf{V}_A^* (in red), and $-\mathbf{V}_A^*$ (in green), all in MVA coordinates. Note the expanded scale for the x components.

We note that, in the wedge-like reconnection geometry, a single ideal HT frame does, strictly speaking, not exist: in a frame moving with the plasma and field in the exhaust the two shocks appear to move away from each other at a speed proportional to the wedge angle.

Another problem is that the procedure for determining \mathbf{V}_{HT} should ideally include the tangential, but not the normal, electric field. As we shall see in section 2.7, a normal electric field is present in this event, allowing slippage of the plasma relative to the magnetic field and thus weakening the magnetic coupling between different layers within the event. One possible effect of such slippage could be to decrease the plasma speed in the exhaust jets. Still another factor degrading the quality of the HT frame could be rapid changes of the magnetopause speed.

In spite of these shortcomings, we have used the standard HT frame determination to obtain the best fit to the theoretical model of steady, field-aligned flow. The HT frame velocity found for the whole event is $\mathbf{V}_{HT} = (-14.1, -12.6, -217.5)$ km/s in MVA coordinates. The smallest purely statistical error occurs in \mathbf{V}_{HTx} ; it is ± 2.5 km/s.

2.4. Walén Relation

In this section, we examine to what extent the plasma flows are Alfvénic. In the top part of Figure 4, we again show the number density (Figure 4a) and the field magnitude (Figure 4b). Figure 4c shows that the normal field component, while positive on average, exhibits substantial fluctuations. In particular, a large positive peak reaching about 20 nT occurs at 17:00:30 UT. Figures 4d and 4e show the pressure anisotropy factor, combined for ions and electrons, $\alpha = (p_{\parallel} - p_{\perp})\mu_0/B^2$, which is strongly variable, and the combined plasma $\beta = p 2\mu_0/B^2$, which changes from being very small in the magnetosphere to values of order 1 in the

magnetosheath, with large values in the middle of the event. The bottom part of Figure 4 shows the results of the Walén test for the interval 16:58:55–17:01:20 UT, i.e., the same interval as that used for the MVA in Figure 3, in the form of a component-by-component comparison between $\mathbf{V}' \equiv (\mathbf{V} - \mathbf{V}_{\text{HT}})$, the plasma velocity in the deHoffmann-Teller (HT) frame, and the Alfvén velocity, corrected for pressure anisotropy, such that $\mathbf{V}'_{\text{A}} = \mathbf{B}[(1 - \alpha)/\mu_0\rho]^{0.5} = \mathbf{V}_{\text{A}}(1 - \alpha)^{0.5}$ [e.g., Paschmann and Sonnerup, 2008]. The values of the anisotropy factor α are taken from Figure 4d. They are based on the perpendicular and parallel combined ion and electron temperatures shown in Figure 2.

Because \mathbf{V}' and \mathbf{V}'_{A} are anticorrelated in the outer part of the magnetopause, the \mathbf{V}'_{A} time series was split at 17:00:30 UT and the outer part replaced by $-\mathbf{V}'_{\text{A}}$ (in green). A few points are missing in the \mathbf{V}'_{A} trace because, for $\alpha > 1$, the correction factor $(1 - \alpha)^{0.5}$ becomes imaginary. The fairly good agreement, except for the first 25 s, indicates that, as seen in the HT frame, the flows are indeed approximately field aligned and Alfvénic. The large discrepancy between the z components (Figure 4h) at the beginning of the interval is in part caused by using the proton mass, rather than the true effective ion mass in calculating the Alfvén speed. More discussion of this topic will be given in section 3.2.

Where the components of \mathbf{V}' and \mathbf{V}'_{A} are correlated (anticorrelated), the normal (x) component of \mathbf{B} and of \mathbf{V}' must have the same (opposite) signs. Since we have already determined B_x to be positive throughout, it follows that there must be a flow reversal, with the net normal flow positive (directed outward) in the magnetospheric part of the magnetopause (Shock 1), and negative (directed inward) in the magnetosheath part (Shock 2). There is direct evidence for this reversal in Figure 4f, showing that V'_{x} , the normal velocity in the HT frame, changes from positive to negative values in the event.

The switch-off shock, i.e., the special type of slow MHD shock in which the downstream tangential field is zero, is a close relative of the RD in the sense that both have Alfvénic upstream states. However, their downstream states are different: for the RD it remains Alfvénic but for the switch-off shock it is sub-Alfvénic. Contrary to the ideal RD, the switch-off shock, or indeed any slow-mode shock, does not precisely obey the standard Walén relation (for a generalized version of this relation, applicable to nonresistive MHD switch-off shocks, see section 4.2). In the downstream region of each shock, the Alfvén speed as well as the plasma flow speed evaluated in the HT frame are small and fluctuating. Their ratio is therefore poorly determined. For this reason, the approximately Alfvénic behavior shown in Figure 4 cannot be used to decide the issue of RD versus switch-off shock. More decisive items, pointing firmly to switch-off shocks, are the near switch-off of the tangential field as the plasma enters the exhaust jet from its two sides, as well as the increases in density and temperature seen across each boundary of the jet. However, note that such behavior for an RD, while unlikely, can perhaps not be entirely excluded, when allowance is made for anisotropic pressure effects (see section 4.3).

2.5. Magnetopause Motion and Thickness

As this is an outbound crossing, the normal component of the magnetopause velocity must have been directed inward. Consistent with this requirement, the average normal component of the HT frame velocity is negative, $V_{\text{HTx}} = -14.1$ km/s (see section 2.4). This speed, together with the durations (specified later on in Table 1), implies thicknesses of Shock 1 and Shock 2 of ≈ 1227 km = $12.3 \lambda_i$ and ≈ 338 km = $6.2 \lambda_i$, respectively. The nominal ion inertial length was $\lambda_i = 100$ km for Shock 1 and 55 km for Shock 2. These values are based on nominal effective ion masses of 2.39 amu and 1.09 amu, respectively (see sections 3.1 and 3.2). Since these thickness estimates are proportional to V_{HTx} , they have uncertainties associated with both the normal vector and the HT frame velocity vector. Individual structures seen in the event may in reality move faster or more slowly, as a result of a variable magnetopause speed.

The time series of magnetic field, density, and z velocity in Shock 1 show indications of back and forth motion, which may be a factor contributing to the large apparent thickness and to the aforementioned low HT correlation. The peak in B between the two minima, which has a magnitude of some 25 nT can be interpreted as a quick earthward motion of the magnetopause over the spacecraft so that it begins entering Shock 2, followed by an equally quick sunward motion, bringing it back into the low field region. Finally, rapid earthward motion again causes the spacecraft to traverse Shock 2 entirely and enter the magnetosheath. The large magnitude of the field peak and the behavior of B_z , which becomes negative in the rising part of the peak and then returns to near zero in the falling part, both support this explanation. But the x component of the velocity does not show any indication of such reversals of the motion. As mentioned already, B_x also has a substantial peak. This peak is inconsistent with simple in-out motion of a one-dimensional (1-D) structure; it requires a substantial local 2-D or 3-D deformation of the discontinuity.

2.6. Reconnection Rate and Geometry

The dimensionless reconnection rate is often expressed as the inflow Mach number $M_0 = V'_x/V_{A\perp}^*$. Here the inflow speed V'_x is evaluated in the HT frame and the upstream perpendicular Alfvén speed is $V_{A\perp}^* = B_{\perp}[(1 - \alpha)/(\mu_0\rho)]^{0.5}$, in which the field component B_{\perp} is perpendicular to the x axis, i.e., it is tangential to the magnetopause. For a switch-off shock (and also for an RD), this rate simplifies to $M_0 = B_x/B_{\perp}$, i.e., the ratio of upstream normal to perpendicular field component. With $B_x = 3.0$ nT, the resulting reconnection rate is $M_0 = 0.061$ for Shock 1 and $M_0 = 0.085$ for Shock 2, with an average of 0.073. To illustrate the inherent uncertainties associated with these numbers, one can use the individual upstream measured B_x values instead (see Table 1), with the result $M_0 = 0.070$ for Shock 1 and $M_0 = 0.077$ for Shock 2. An alternative approach is to express the reconnection rate in terms of the electric field component along the reconnection line (the X line). In our event, the field line motion in the exhaust should, in the ideal Petschek configuration, be $V_{HTz} = -217.5$ km/s with the corresponding reconnection electric field $E_0 = E_y = -V_{HTz}B_x = 0.65$ mV/m. In reality, the value may be less, as a result of southward X line motion and of field line slippage (see section 3.3).

An average magnetopause speed of 14.1 km/s gives a total width of the event of $\Delta x = 1565$ km. A rough estimate can also be obtained for the distance L_0 from the spacecraft to the X line. Using mass conservation in a simple wedge geometry formed by two switch-off shocks leads to an equation of the form $N_1 V_{x1} L_0 = N_2 V_{x2} \Delta x_{\text{Shock}\#}$ for each shock, with $\Delta x_{\text{Shock}1} + \Delta x_{\text{Shock}2} = \Delta x = 1565$ km (subscripts 1 and 2 denote upstream and downstream values, respectively). The result is $L_0 \approx 19,183$ km $\approx 3.0 R_E$, which gives a shock angle of 4.7° .

Since one expects the field geometry to be more cusp-like than wedge-like near the reconnection site, this L_0 is probably an underestimate of the actual distance. The spacecraft was located $3.8 R_E$ below the GSM equator so that the X line could therefore have been located near the GSM equator. Using our L_0 value, together with magnetic flux conservation between a shock and its adjoining separatrix, we can also estimate the separatrix location to be 1170 km upstream of Shock 1 and 1630 km upstream of Shock 2. The angle between the two separatrices is estimated to be $\theta_{\text{sep}} = 13^\circ$. With a constant magnetopause speed of 14.1 km/s, the corresponding time shifts upstream of the shocks would be 1.4 min and 1.9 min, respectively. As mentioned already, the two shocks may in reality have been moving at different speeds. No clear signatures of the separatrices have been found in the data from this event [Øieroset et al., 2015].

2.7. Hall-Induced Magnetic and Electric Fields

In addition to the standard, in-plane, X type magnetic geometry in Figure 1, symmetric reconnection in a collisionless plasma should also exhibit a characteristic quadrupolar pattern of the out-of-plane magnetic field component [Sonnerup, 1979], i.e., in our case, the B_y component, as illustrated in Figure 5a. This behavior has its origin in the diffusion region surrounding the magnetic X point, where incoming ions from both sides become unfrozen from the magnetic field and slow down over a distance of the inertial or thermal ion scale size, whereas the electrons become unfrozen only on the much smaller electron scales. The result of this differential motion is Hall currents directed away from the current sheet on both sides and associated Hall electric fields, $\mathbf{j} \times \mathbf{B}/Ne$, directed toward the current layer on each side.

Closure of the Hall currents is thought to occur in “Hall loops” that may extend along the magnetopause out to substantial distances away from the diffusion region; these loops are responsible for the overall quadrupolar, out-of-plane, magnetic field configuration. Because field lines tend to remain equipotentials, field-aligned layers containing strong normal electric fields, of the same polarity as the Hall electric field in the diffusion region, may also persist out to substantial distances.

Hall effects could, in principle, also be present as an intrinsic part of the slow shocks that become established some distance away from the reconnection site. The resulting out-of-plane magnetic field would have polarity opposite to that associated with the aforementioned Hall loops [Hau and Sonnerup, 1990; Sharma et al., 2008]. The result would be an S-shaped B_y plot (or tangential hodogram) associated with each combined Hall loop and shock. The presence of a guide field or of different plasma/field properties in the two inflow regions can introduce asymmetry of the Hall loops. The presence of cold ions or of heavy ions can also influence the strength and configuration of the Hall signatures.

Some aspects of the behavior described above have since been verified both in numerical simulations [Birn et al., 2001; Karimabadi et al., 2004] and in observations of reconnection in the geomagnetic tail [Nagai et al., 2001; Øieroset et al., 2001] and in the magnetosheath [Phan et al., 2007]. Simulations and observations of asymmetry resulting from the presence of a guide field have been described, for example, by Eastwood et al. [2010]. Simulations of various asymmetries of the inflow plasma and fields have been reported

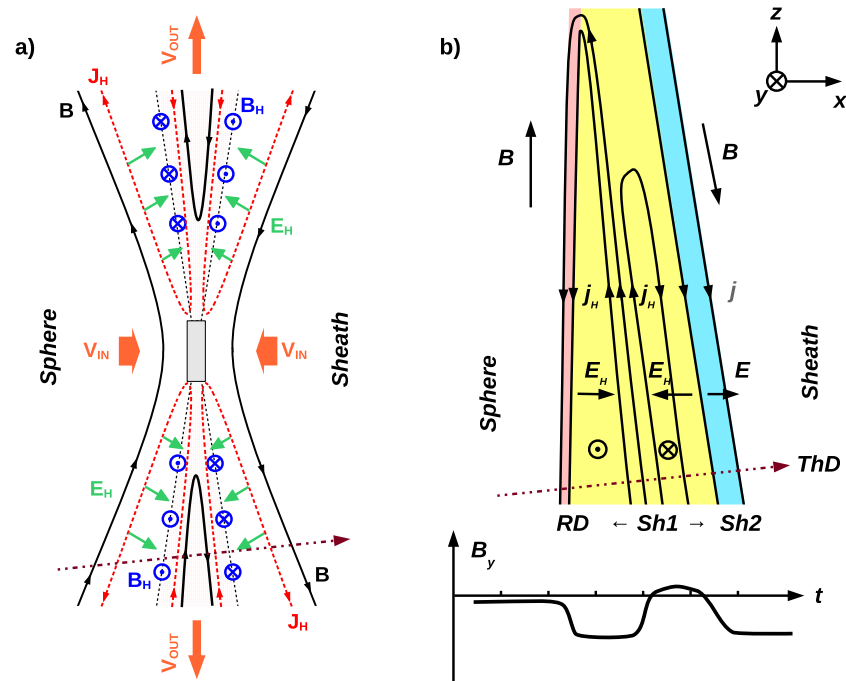


Figure 5. Schematic diagrams of Hall effects in the xz plane. (a) Symmetric situation with its quadrupole B_y configuration [after Teh *et al.*, 2011]. (b) In our event, the Hall effects appear to be mainly confined to Shock 1 (Sh1), including its attached rotational discontinuity (RD). Two Hall current loops of opposite polarity and corresponding Hall electric fields (as seen in the spacecraft frame) appear to be present, as can be inferred from $\mu_0 j_z = dB_y/dx$. In Shock 2 (Sh2), the current inferred from the low-resolution data is on average mostly unidirectional and the electric field points sunward; their possible relation to Hall effects in the diffusion region, the latter located above the field of view, remains unclear.

by Malakit *et al.* [2010], a combination of both by Pritchett and Mozer [2009], and the influence of cold ions by Toledo-Redondo *et al.* [2015]. But we are not aware of simulations that mimic the plasma and field conditions present in our event sufficiently closely to permit a meaningful quantitative comparison. In particular, the apparent guide field, formally some 9.9 nT in our event (a value based solely on the magnetic field vectors on the two sides), is not a real guide field. It is brought to essentially zero between the two shocks, whereas simulations with an added true guide field show an enhancement of that field component.

We now ask if any of the basic magnetic and electric signatures described above are in evidence during our crossing. Figure 6 shows the relevant data. The behavior of the out-of-plane magnetic field component, B_y , is shown by the green curve in Figure 6c. It displays bipolar behavior in the crossing but also a net change of B_y from one side to the other, associated with the net field rotation of 152° , i.e., not fully 180° , across the entire event. The bipolar part starts at about 16:59:10 UT when, beginning from a small negative value, B_y rapidly turns more negative and then returns to zero more gradually, with evidence of some back and forth motion of the magnetopause. This behavior is consistent with the spacecraft crossing the Hall loop on the magnetospheric side. The abrupt crossing of the earthward branch of this loop appears to be in the form of the RD, seen around 16:59:10 UT, with a duration of about 10 s and a corresponding estimated nominal width of $1.4 \lambda_i$. In this RD, the current is directed southward, i.e., away from the reconnection site, as expected from the theoretical scenario described above. This intermediate-mode structure should be located upstream of, but adjoining, the leading edge of the switch-off shock, as it is indeed seen to be. The second branch of the Hall loop appears to occupy a broad part of the region within Shock 1. The green curve in Figure 6c then enters a region of small, mainly positive, B_y until about 17:00:45 UT, i.e., close to our chosen downstream point of Shock 2. After that, the green curve crosses over to negative B_y values and then continues to decrease, along with B_z , until the two settle down to their respective negative levels in the magnetosheath. The magnetosheath level for B_y is nearly the same as that observed immediately downstream of the RD.

The positive part of the overall bipolar signature seen in B_y is located in the downstream half of Shock 1; it does not appear to be a consequence of the spacecraft crossing a Hall loop associated with the magnetosheath side. Instead, the deviation of B_y from zero within Shock 1 could possibly be an intrinsic part of the shock

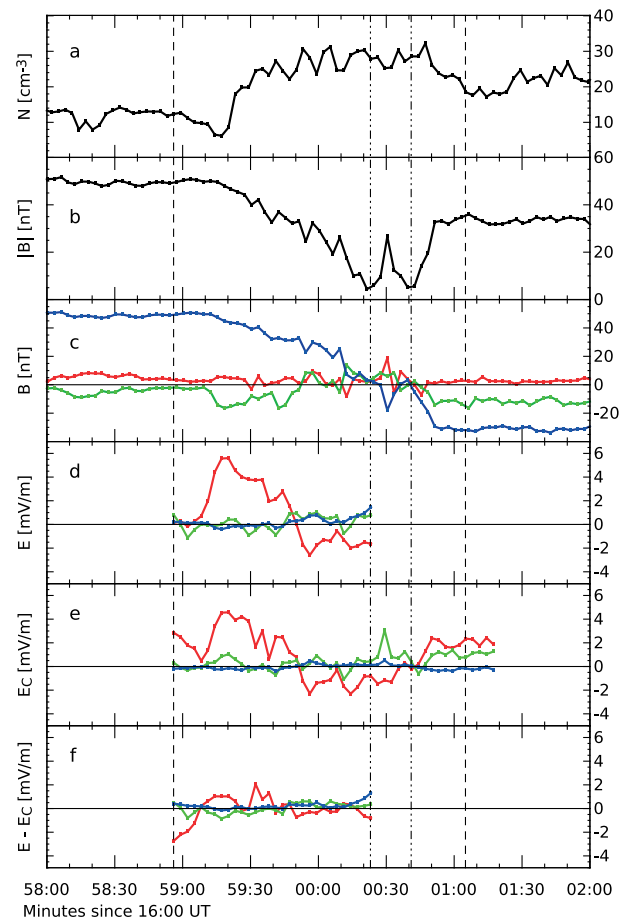


Figure 6. Electric fields. For context, the figure again shows (a) density; (b) magnetic field magnitude and (c) components in MVA coordinates. (d) Spin-resolution electric field data, as measured by EFI, with a 1 mV/m corrective offset added to the x component. The EFI data, which contain the assumption $\mathbf{E} \cdot \mathbf{B} = 0$, were continuously available only for the time interval corresponding to Shock 1. (e) Convection electric field $\mathbf{E}_C = -(\mathbf{V} \times \mathbf{B})$; (f) the difference between the two.

structure itself, as discussed by [Hau and Sonnerup, 1990; Sharma et al., 2008]. The S-shaped, low-resolution tangential hodogram trace in the right half of Figure 3b illustrates that the bipolar behavior of B_y is indeed mainly confined to the Hall loop and the adjoining Shock 1. By contrast, in Shock 2 the low resolution field appears more or less confined to a plane. Excluding the effects of the field peak, marked by blue dots in the low resolution hodograms in Figure 3b, this behavior can be seen from the, only weakly curved, lower part of the tangential hodogram trace. This part of the trace describes Shock 2, but in the low resolution data, the rapidly changing part actually contains only one, possibly space/time-aliased, point. At low resolution, there is therefore no convincing indication of an RD or an associated Hall loop on the magnetosheath side. But, as discussed below, this conclusion no longer holds at the higher resolution. The in-plane currents causing the behavior of the low resolution B_y are shown schematically in Figure 5b. The blue region in this figure, which marks Shock 2, contains a unidirectional in-plane current component. This current is the projection of the main shock current onto the xz plane. It is the result of the total field rotation across the event being less than 180° .

If one instead examines the high-resolution tangential hodogram in Figure 3a, one can see a small RD-like field rotation (at the bottom of the hodogram trace) that could perhaps be interpreted as caused by a Hall loop on the magnetosheath side. The location of this RD just upstream of Shock 2, and the in-plane current direction in it (away from the reconnection site), are both features consistent with this interpretation. The fact that this RD is not evident in the low-resolution data could be a consequence of Shock 2 moving more rapidly than Shock 1. Such behavior could, at least in part, also explain the large asymmetry evident in the

time series. As an aside, we note that, throughout the event, Hall effects must also be present in the magnetic field fluctuations, some of which have large amplitude and persist even in the low-resolution data.

Figures 6d and 6e provide information about the electric field measured by EFI (data from this instrument were continuously available only prior to, and during Shock 1), followed by the convection electric field $\mathbf{E}_c = -(\mathbf{V} \times \mathbf{B})$. Both fields are evaluated in the frame moving with the spacecraft, with components in the MVA system. Use of the spacecraft frame is based on the assumption that the reconnection site does not move along the magnetopause surface during the crossing. Note also that magnetopause motion along the normal direction does not influence the normal electric field.

The z components of the EFI electric field are very small. The y components are also small but more variable during the passage through Shock 1. For a strictly two-dimensional, steady configuration, at rest in the spacecraft frame, this field component would be constant and equal to the reconnection electric field. Most of the variability is in the x component. A sharp rise in this component, up to a value of nearly +6 mV/m occurs at the RD, where it causes an increased plasma velocity along x and a drift of the plasma in the negative y direction (see Figures 4f and 4g). The positive E_x field persists at a somewhat lower level well into Shock 1, where the density increases rapidly. It is then followed by a sign reversal at about 16:59:50 UT and a continued decrease until it reaches a level of about -2 mV/m, where it remains until the end of Shock 1.

The convection electric field, which is shown in Figure 6e for the entire event, has similar behavior. In particular, the E_{cx} component shows a clear bipolar feature, with the electric field pointing toward the center of Shock 1 on its two sides. A small positive pulse in the y component, E_{cy} , at the beginning of the shock can also be seen, presumably associated with the pulse of increased V_x . This latter pulse is visible in Figure 4f. As a consequence of mass conservation (for details, see Figure 7e), it leads to the minimum in the plasma density, seen at around 16:59:15 UT (see Figure 6a). Such density minima, assumed to be located near the separatrices, have been seen in simulations, even at substantial distances away from the reconnection site [Shay *et al.*, 2001], and also in observations near the reconnection site [Mozer *et al.*, 2002; Khotyaintsev *et al.*, 2006]. However, our minimum appears to coincide with an abrupt field rotation (RD) immediately upstream of Shock 1 rather than with the separatrix, which we predict should have been encountered more than a minute earlier (see section 2.6). In Shock 2, E_{cx} gradually reverses sign and then settles down to a positive value of about 2 mV/m in the magnetosheath.

In Figure 6e, the E_{cy} component at the upstream reference time of Shock 1 appears small but can be calculated from the velocity and field data in Table 1 to be +0.30 mV/m. If the magnetopause were at rest in the spacecraft frame, this number should have been approximately equal to the reconnection electric field, estimated in section 2.6, to be +0.65 mV/m. The discrepancy could be accounted for by assuming that the earthward magnetopause speed at the upstream reference time was only 7 km/s.

The difference between the field recorded by EFI and the convection field \mathbf{E}_c is shown in Figure 6f. This panel should, in principle, indicate deviations from the simple frozen field condition. Upstream of Shock 1 there are large, unexplained differences, in particular, in the x components. Within Shock 1 the agreement is better, indicating that the electric field there is mainly a convection field. The differences (e.g., the positive pulse seen in the x component around the density minimum) could come from the Hall term in the generalized Ohm's law.

The asymmetry of the Hall current loops, resulting from the presence of a regular guide field, is such that the two diagonally opposite Hall loops, within which the out-of-plane magnetic field is augmented by the guide field, tend to become wider and stronger, while the other two loops become thinner and weaker [e.g., Eastwood *et al.*, 2010]. In our event, the direction of the formal guide field is such that the magnetosphere side should have the wider and stronger region of out-of-plane field, and that is indeed what is seen. But since the guide field model does not describe the observed near switch-off of the tangential field, it is not clear to what extent these simulations are relevant.

The plasma/field asymmetry usually present at the magnetopause usually tends to make the two Hall current loops on the magnetospheric side weaker and the two on the magnetosheath side stronger [Malakit *et al.*, 2010]. This is the opposite of what is seen in our event. For a possible explanation of this apparent disagreement, see section 3.2.

Table 1. Measured Reference States for Shock 1 and Shock 2^a

Reference	Shock 1		Shock 2	
	Upstream	Downstream	Downstream	Upstream
UT	16:58:56	17:00:23	17:00:41	17:01:05
N	12.33	27.81	28.51	18.45
\mathbf{B}	[3.44, -1.97, 49.27]	[2.38, 3.65, 2.63]	[1.58, 1.28, -1.76]	[2.70, -15.30, -31.93]
\mathbf{V}	[4.58, -56.63, -24.28]	[-21.59, 23.20, -209.09]	[-13.96, 15.08, -198.44]	[-20.74, 53.64, -41.63]
\mathbf{V}'	[18.72, -44.03, 193.20]	[-7.44, 35.79, 8.39]	[0.19, 27.67, 19.05]	[-6.59, 66.23, 175.85]
\mathbf{V}_A	[21.36, -12.25, 306.29]	[9.85, 15.10, 10.90]	[6.45, 5.23, -7.20]	[13.74, -77.77, -162.27]
α_i	-0.003115	-2.522344	16.385667	-0.175974
α_e	-0.000368	0.216435	0.223229	-0.011963
β_i	0.0451	59.5719	226.6987	0.7252
β_e	0.00265	16.76943	60.35502	0.16282
p_B	0.9720	0.0103	0.0029	0.5017
$p_{\perp i}$	0.0444	0.6814	0.6774	0.3734
$p_{\perp e}$	0.00268	0.18038	0.17630	0.08348
$p_{\parallel i}$	0.0383	0.6294	0.7716	0.1968
$p_{\parallel e}$	0.00196	0.18485	0.17759	0.07148
M_{A1}^*	0.647	0.979	nan	0.956
M_{A1}	0.648	1.780	3.056	1.042

^aDensities N are in $1/\text{cm}^3$; magnetic fields \mathbf{B} in nT; velocities \mathbf{V} , \mathbf{V}' , and \mathbf{V}_A in km/s; pressures p_B , p_{\perp} , and p_{\parallel} in nPa. Vector quantities are in MVA coordinates. Ion plasma data and Mach numbers assume all particles to be protons. Velocities $\mathbf{V}' = \mathbf{V} - \mathbf{V}_{\text{HT}}$ as well as corresponding Mach numbers M_{A1}^* and M_{A1} (in the HT frame) are based on $\mathbf{V}_{\text{HT}} = (-14.1, -12.6, -217.5)$ km/s. In this table, and elsewhere, the high precision given for the data does not represent actual accuracy; it is retained to enable numerical checking.

3. Jump Conditions

In this section, we evaluate the conservation laws from the upstream side (subscript 1) to the downstream side (subscript 2) of each shock. The purpose is to examine how well the measured data are consistent with, or can defensibly be made consistent with, the spacecraft traversing two, basically one-dimensional, slow-mode shocks, both very near the switch-off state.

Table 1 forms the basis for the calculations. It gives an overview of the measured plasma and field conditions upstream and downstream of each shock. Except for the number density in the early part of Shock 1, ion parameters in the table have been evaluated from the ESA instrument response, using the standard assumption that all ions are protons, which in reality is not the case for either shock, especially not for Shock 1. Vector quantities in the table are given in MVA coordinates. As already mentioned, the RD at the upstream edge of Shock 1 marks the onset of the Hall-induced y component of the magnetic field. The RD does not satisfy coplanarity and, strictly speaking, is not a proper part of Shock 1. However, to check the thermodynamic part of the jump conditions, we have nevertheless placed the upstream state of Shock 1 well ahead of the RD, where conditions are relatively steady. Note that $\mathbf{V}' \equiv (\mathbf{V} - \mathbf{V}_{\text{HT}})$ is the plasma velocity in the HT frame and that some of the downstream parameters in the table are numerically small and have large uncertainties. As a result, some ratios of small numbers given in the table, such as α_2 and the downstream Alfvén Mach numbers (in the HT frame), are not meaningful and will not be used. Note that M_{A1} and M_{A1}^* in Table 1 are the Alfvén Mach numbers based on \mathbf{V}_A and \mathbf{V}_A^* , respectively (see section 2.4), and on the invalid assumption that all ions are protons.

3.1. Thermodynamic Quantities

The jump conditions for the thermodynamic quantities across each shock will now be checked against simple MHD predictions. Note that the actual HT frame velocity vector is not needed in performing this check. We make use of the simplest possible description of the shocks, namely, in terms of single-fluid MHD with isotropic pressure, with temperature given by $p = NkT$, and with the ratio of specific heats, $\gamma = 5/3$, for a monoatomic gas. The general properties of slow MHD shocks were discussed early on by *Kantrowitz and Petschek* [1966].

Table 2. Predicted and Observed Pressure, Temperature, Density, and Proxy Entropy Ratios^a

	Shock 1 $\beta_1 = 0.0478$		Shock 2 $\beta_1 = 0.8880$	
	Predicted	Observed	Predicted	Observed
p_2/p_1	21.92	18.88	2.25	2.25
T_2/T_1	9.37	8.35	1.45	1.46
N_2/N_1	2.34	2.26	1.47	1.55
S_2/S_1	5.31	4.85	1.12	1.08
$k_v^{-2}k_m$	2.39		1.09	

^aRequired mass and/or velocity correction factors are k_m and k_v such that $k_v^{-2}k_m = 1/(M_{A1}^{*2})$, with M_{A1}^* taken from Table 1.

In our application, we treat the observed shocks as switch-off shocks. Since there are no tangential stress terms at the downstream end of such a shock, the upstream tangential stresses must also add to zero, i.e., $\rho V'_{x1} V'_{z1} = (1 - \alpha_1) B_x B_{z1} / \mu_0$, with a similar formula for the y component. The upstream (and downstream) flow is assumed to be field aligned in the HT frame, which then allows the two tangential components to be reduced to the switch-off condition $M_{A1}^{*2} = 1$. We further assume the shocks to have a very small upstream ratio of normal to tangential magnetic field. With these assumptions, which are reasonably well satisfied for our two shocks, the MHD jump condition for normal stresses and for total energy simplify to $p_1 + p_{B1} = p_2$ and to $c_p T_1 + (1/2) V_{A1}^{*2} = c_p T_2$, respectively. In terms of the upstream plasma beta, $\beta_1 = p_1 2 \mu_0 / B_1^2$ and the gas law, we then find

$$\left. \begin{aligned} p_2/p_1 &= 1 + 1/\beta_1 \\ T_2/T_1 &= 1 + (2/5)/\beta_1 \\ N_2/N_1 &= (\beta_1 + 1)/(\beta_1 + 2/5) \\ S_2/S_1 &= (p_2/p_1)/(N_2/N_1)^{5/3} \end{aligned} \right\} \quad (1)$$

Note that the symbol S does not denote the actual entropy; instead, it is the usual proxy, $S = p/N^{5/3} = T/N^{2/3}$.

With the upstream values $\beta_1 = \beta_{i1} + \beta_{e1}$ taken from Table 1, the formulas (1) predict the ratios listed in Table 2. The observed values, also taken from Table 1, are given for comparison. In arriving at the numbers in the “observed” columns of Table 2 from the data in Table 1, we used $p = (\rho_{\parallel} + 2\rho_{\perp})/3$ and included contributions from both electrons and ions.

Although the predicted numbers in the table do not agree precisely with the measured values, the simple formulas above demonstrate that the very different behavior seen in Shock 1 and Shock 2 is determined mainly by the large difference in their upstream β values. The small β_1 for Shock 1 leads to large pressure, temperature, and entropy ratios whereas, for Shock 2, β_1 is of order 1, which produces much smaller ratios. The rough agreement between the measured ratios and the simple predictions for switch-off shocks provides evidence that our interpretation in terms of such shocks is justified. The required mass and/or velocity correction factors, k_m and k_v , must be such that the true upstream value of M_{A1}^{*2} is equal to one, as required for a switch-off

Table 3. Predicted and Observed Pressure, Temperature, Density, and Proxy Entropy Ratios for Shock 1, After Ion Pressure Correction by the Factor k_p

	Shock 1 $\beta_1 = 0.0578$	
	Predicted	Observed
p_2/p_1	18.22	18.22
T_2/T_1	7.88	8.06
N_2/N_1	2.31	2.26
S_2/S_1	4.51	4.68
k_p	1.27	

shock. This condition leads to the values of $k_v^2 k_m$ given in the bottom line of Table 2. We refer to the k_m values 2.39 and 1.09 that correspond to $k_v = 1$ as the “nominal” values. They may differ from their true values as a result of possible errors in \mathbf{V}_{HT} and, for Shock 1, errors in the plasma velocities caused by the unmeasured cold plasma population (see section 3.2 below).

The agreement between prediction and measurement in Table 2 is by no means perfect. The absence of complete total pressure balance, evident in Figure 2i, suggests that, at least for Shock 1, the measured ion pressures may be underestimated by the ESA instrument. We can attempt to correct for this defect in a simple manner by multiplying the ion pressure by a correction factor, k_p so that $p_{corrected} = k_p p_i + p_e$. Such a correction will influence not only the measured pressure ratio, 18.88 for Shock 1, but also the plasma beta used in the predictive formulas: $\beta_{1corrected} = k_p \beta_{i1} + \beta_{e1}$. We can then determine k_p by requiring the predicted and measured pressure ratios to agree, after both have been corrected. The result for Shock 1 is $k_p = 1.27$, along with the modified numbers given in Table 3. For Shock 2, the predicted and measured pressure ratios in Table 2 are the same so that no correction is needed ($k_p = 1$).

It is seen that the pressure correction for Shock 1 brings measurements and predictions closer together. But some discrepancies remain for both shocks and must have different explanations. Deviations from our simple quasi one-dimensional, time-independent, model could contribute both to the pressure corrections needed and to the remaining discrepancies, and so could the pressure anisotropy. There are also further remaining uncertainties in the measurements, associated with the presence of heavy ions [see *Paschmann et al.*, 1986, Appendix] and with the effective low-energy cutoff of the ESA instrument.

3.2. Effective Ion Mass

The Mach numbers given in Table 1 are based on the assumption that all ions are protons, that the measured plasma velocities need no corrections, and that our HT frame velocity is accurate. The fact that M_{A1}^* in the table, which should equal to one for a switch-off shock, is less than one for both shocks makes clear that, either a mass correction $k_m = m_{effective}/m_{proton}$, caused by the presence of some heavy ions, and/or a velocity correction, $k_v = V'_{true}/V'_{measured}$ (evaluated in the HT frame), is required. At the upstream state of Shock 1, a correction of the measured velocity could be needed because of differential motion along the magnetic field between the measured ions and the cold, unmeasured ions. Assuming V_{HT} to be correct, this correction factor could be in the range $0.98 < k_{v1} < 1.30$ and still leave the cold ion energy below the effective ESA low-energy cutoff potential. This range results from a combination of the nominal instrument cutoff and the spacecraft potential, together about 10 eV. With our value $k_v^2 k_m = 2.39$ (see Table 2), the effective mass ratio for Shock 1 could therefore, in principle, be anywhere in the wide range $1.41 < k_m < 2.49$, which has substantial overlap with the range $1.31 < k_m < 2.30$ reported by *Borovsky et al.* [2013] for events where the magnetospheric side of the magnetopause is immersed in a plasmaspheric plume. For example, the upper limit, $k_m = 2.30$, of the observed range would require the velocity correction factor to be $k_v = 1.02$ in our event. This factor is to be applied to the upstream plasma velocity V' for Shock 1, given in Table 1, which requires a field-aligned velocity adjustment of only about 4 km/s. This adjustment could in reality have its cause, either in errors caused by the unmeasured ions or in errors coming from the frame velocity determination, \mathbf{V}_{HT} .

For Shock 2, the plasma velocity was presumably well determined by ESA so that $k_v = 1$, provided that our V_{HT} is correct. The effective mass factor then is $k_m = 1.09$ (see Table 2), which corresponds to an admixture of 3% He^{++} . This percentage is in the range of values typically seen in the solar wind. Errors in the field-aligned portion of \mathbf{V}_{HT} cannot be excluded but seem to be small, given this result.

A consequence of the “nominal” k_m values (i.e., assuming $k_v = 1$) we have deduced for the two shocks is that the actual mass density would be $\rho = 20.1$ amu in the magnetosheath and $\rho = 29.5$ amu in the magnetosphere. Since the inflow into a switch-off shock is Alfvénic, we conclude that the mass flux into the reconnection wedge from the magnetosphere was some 20% larger than that from the magnetosheath. Herein lies the likely explanation for the approximate Petschek-like symmetry observed in the magnetic field configuration of our event. Also, the disagreement with the *Malakit et al.* [2010] simulations mentioned in section 2.7 is potentially removed: the stronger Hall loops could well be located on the magnetospheric side, as appears to be the case in our event.

3.3. Tangential Velocity Jumps

As can be seen in Table 1, the tangential plasma velocity components on the two sides of the event (i.e., the upstream states of the shocks) show large differences: 110.3 km/s in the y components and 17.4 km/s in the z components. This fact indicates, either that the magnetic configuration was undergoing rapid temporal changes or that the frozen field condition does not hold across the reconnection layer. It appears likely that the latter is the case and is a direct consequence of normal electric fields remaining in the HT frame, thereby causing slippage of the various plasma layers relative to each other, as already discussed in section 2.3.

The average of the plasma flow velocities at the two field minima is within 5.4° of the negative MVA z direction, with z component $V_z = -203.8$ km/s (see Table 1). These results suggest that the X line orientation was fairly close to the MVA y axis, thus allowing us to focus on the changes in V_z . If no slippage in the z direction occurs, and if the measured plasma velocity upstream of Shock 1 is correct, then $\Delta V_z = 184.8$ km/s should be exactly Alfvénic, which would require $k_m = 2.76$. This value is outside the allowable range, $1.41 < k_m < 2.49$, given in section 3.2. For Shock 2, we have $\Delta V_z = 156.8$ km/s, which would require $k_m = 1.27$, a number that is unacceptably high for the solar wind plasma. The conclusion is that slippage of the plasma layers relative to each other must be present. This conclusion is independent of the quality of the HT frame determination.

4. Dissipation Mechanisms

In this section, we examine the possible roles played by resistive or viscous effects within each shock. Such effects could be the result of fluctuations in the electric and magnetic fields. That such fluctuations are present and have substantial amplitudes is evident from the hodogram sets in Figure 3.

4.1. Mass Conservation

In a steady state, conservation of mass across a one-dimensional (1-D) structure requires

$$\rho V'_x = \text{const} = \rho_1 V'_{x1} \quad (2)$$

Here the subscript 1 refers to the upstream reference state and the absence of a subscript refers to any location within the structure. In our MVA coordinate system, V'_x and V'_{x1} are positive for the first shock and negative for the second shock. All velocities are those in the HT frame, where the flow is, at least ideally, field aligned on the two sides of the shock, although not necessarily within it. From here on, we also assume for simplicity that the effective ion mass remains roughly constant through each shock, although this may in reality not be the case for Shock 1. We can then check how well the mass conservation law holds by comparing V'_x (black curve) to $V'_{x1} N_1/N$ (red curve) in Figure 7e. Although there are some differences between the two curves, caused, for example, by back and forth motion or by variable effective ion mass, we conclude that steady 1-D mass conservation holds sufficiently well so that it can be used in our upcoming examination of Ohm's law and the tangential momentum equation. In particular, mass conservation appears to approximately hold across the density dip at the beginning of Shock 1.

When applied between the upstream and the downstream state of each shock, the mass conservation law can be rearranged to give $M_{A2}^2 = M_{A1}^2 (\rho_1/\rho_2)$. From this formula, downstream Mach numbers, can be calculated from the density ratio and the switch-off condition $M_{A1}^2 = (1 - \alpha_1)$, with the ion pressure in α_1 corrected by the factor k_p . The result for Shock 1 is $M_{A1} = 1.002$ and $M_{A2} = 0.667$; for Shock 2 it is $M_{A1} = 1.090$ and $M_{A2} = 0.877$. Comparison of these numbers with those given in Table 1 illustrates how misleading the Mach numbers calculated from the raw data in the table can be.

4.2. Ohm's Law

From the y component of Ohm's law in its simple MHD form, and Ampère's law, we write

$$V'_z B_x - V'_x B_z = -(\eta/\mu_0) dB_z/dx + B_x dB_y/dx / (Ne\mu_0) \quad (3)$$

Here the first term on the right represents the resistive electric field along y and η is the resistivity. In reality, the resistive term is unlikely to have the simple form given here. The second term on the right is the y component of the Hall electric field (which is nondissipative). Contributions from the electron pressure tensor are assumed to be negligible. From (2) and (3), we find that the tangential components of flow and field are related by

$$\begin{aligned} V'_z &= (B_z/B_x) V'_x - (\eta/\mu_0 B_x) dB_z/dx + dB_y/dx / (Ne\mu_0) \\ &= (B_z/B_x) (\rho_1/\rho) V'_{x1} - (\eta/\mu_0 B_x) dB_z/dx + dB_y/dx / (Ne\mu_0). \end{aligned} \quad (4)$$

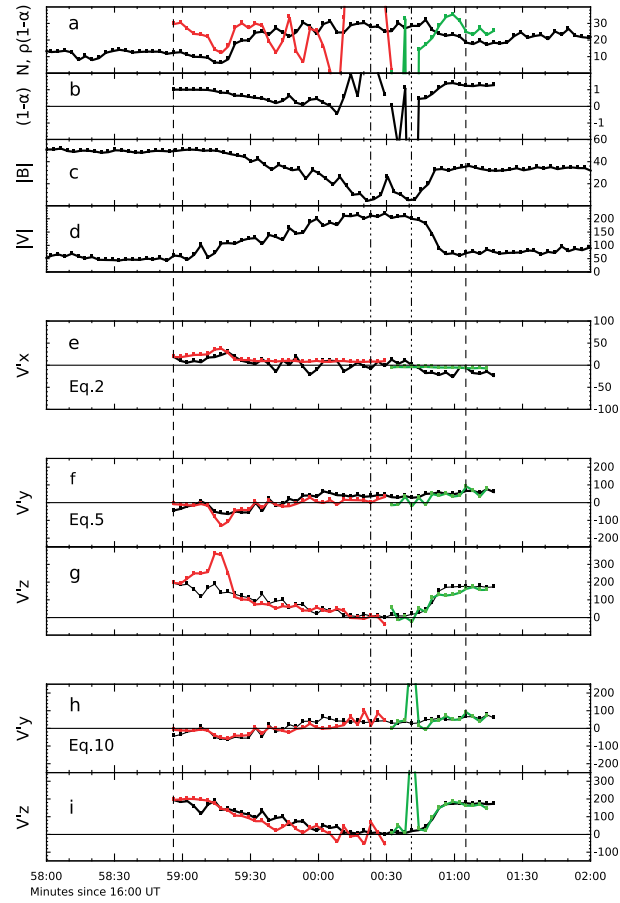


Figure 7. Dissipation mechanisms. First panel block shows reference information: (a) plasma density N (black) and $\rho(1 - \alpha)$ (red for Shock 1; green for Shock 2), both in $1/\text{cm}^3$, with ρ expressed as a modified number density, $k_m N$, where k_m is the nominal ratio of effective ion mass to proton mass ($k_m=2.39$ for Shock 1 and $k_m = 1.09$ for Shock 2), and α is corrected via the ion pressure factor ($k_p = 1.27$ for Shock 1 and $k_p = 1$ for Shock 2); (b) $(1 - \alpha)$ is the factor responsible for much of the large variations in the product $\rho(1 - \alpha)$ (see discussion in section 4.3); (c) magnetic field magnitude (nT); (d) velocity magnitude (km/s). Second block shows mass conservation: (e) V'_x (black) compared with $(N_1/N)V'_{x1}$ (red for Shock 1; green for Shock 2), according to equation (2). Third block shows results from Ohm's law: (f and g) The comparison of $\mathbf{V}' = \mathbf{V} - \mathbf{V}_{\text{HT}}$ (in black) with the rightmost side of equation (5) (red for Shock 1; green for Shock 2). Fourth block shows results from the tangential stress balance: (h and i) same format as Figures 7f and 7g but for equation (10). Velocities (in the HT frame) and fields are in MVA coordinates. Ion pressures, needed for α , are corrected by the factor $k_p = 1.27$ for Shock 1 and uncorrected ($k_p = 1.0$) for Shock 2.

Since we assume the upstream plasma flow to be field aligned, we may then use $V'_{x1}/B_x = V'_1/B_1$ to obtain

$$V'_z = V'_1(B_z/B_1)(\rho_1/\rho) - (\eta/\mu_0 B_x)dB_z/dx + dB_y/dx/(Ne\mu_0). \quad (5)$$

A similar equation applies for the y component of the velocity. Note that the ratio V'_1/B_1 is to be taken as positive for Shock 1 because the flow across it is parallel to the magnetic field and negative for Shock 2 where the flow and field are antiparallel.

The combination of the second and third terms on the right in (5) can, in principle, be evaluated from the data by looking at the difference between the measured values of V'_z on the left side of (5) and the calculated values of $(B_z/B_1)(\rho_1/\rho)V'_1$ on the right side. In comparing these two terms, one can directly use the measured velocities and the numbers given in Table 1, provided the velocity correction factor k_v and the mass correction factor k_m can be considered constant in each shock, as we have done.

Comparison of the left-hand side (black curve) and the first term on the right-hand side (red or green curves) of equation (5) is shown in Figures 7f and 7g. It is based on the upstream reference values listed in Table 1. The discrepancy at the upstream point of Shock 1, which is prominent in Figure 4, is small in the present

plot. Except for the large discrepancy associated with the RD and density dip at around 16:59:15 UT, the fit is reasonably good, implying that, elsewhere, resistive and Hall effects, while perhaps not entirely absent, are small.

To account for the large velocity discrepancy at the density dip (Figure 7g) via the resistive term appears impossible, because a large negative resistivity would be required (dB_z/dx is small and negative). The Hall term has the required negative sign ($dB_y/dx < 0$), but to make it sufficiently large, the width of the RD and associated density dip would be only about 35 km (some $0.4 \lambda_i$). Since the RD/dip duration is about 10 s, the required earthward magnetopause speed would have to be only 3.5 km/s. These requirements are severe but perhaps not entirely unacceptable. At present, they provide our only viable explanation for the large velocity discrepancy seen at the RD/density dip in Figure 7g.

For Shock 2, the deviations between the green and the black points in Figures 7f and 7g cannot be taken as convincing evidence for resistive effects because they do not occur where the current density is large. But note that the shock duration in this case is extremely short, so that only one set of, possibly space/time-aliased, plasma measurements was obtained during the rapid part of the magnetic field ramp.

In the absence of resistivity and Hall terms, equations (5) and (2) can be rearranged into the form of a modified vector Walén relation, namely,

$$\mathbf{V}' = \mathbf{V}'_A \sqrt{\rho_1(1 - \alpha_1)/\rho(1 - \alpha)}. \quad (6)$$

As before, the subscript 1 in this expression refers to the upstream reference state.

Dissipation of some form, and in the appropriate amount, is required for both shocks. If it is not resistivity, then it could perhaps be some form of viscosity (coming from the ion pressure tensor). We examine that possibility next.

4.3. Tangential Momentum Conservation

The role played by viscous-like stresses $F_z(x)$ can be examined by the use of the tangential momentum balance:

$$\rho V'_x (V'_z - V'_{z1}) = (B_x/\mu_0)[B_z(1 - \alpha) - B_{z1}(1 - \alpha_1)] + F_z, \quad (7)$$

where F_z vanishes on both sides (subscripts 1 and 2) of the shock. For a switch-off shock, we have

$$V'_{z1} = B_{z1} \sqrt{(1 - \alpha_1)/\mu_0 \rho_1} \quad (8)$$

$$\rho V'_x = \rho_1 V'_{x1} = B_x \sqrt{\rho_1(1 - \alpha_1)/\mu_0} \quad (9)$$

By the use of (8) and (9), along with the assumption of field-aligned flow at the upstream station, we can rearrange (7) to become

$$V'_z = V'_1(B_z/B_1)(1 - \alpha)/(1 - \alpha_1) + F_z/\rho_1 V'_{x1} \quad (10)$$

A similar equation applies for the y component V'_y . As in (5), the sign of V'_1/B_1 must be made negative for Shock 2.

In the absence of viscous stresses, the first term on the right in (10) must balance the term on the left. In comparing the two terms, the velocity correction factor k_v can again be ignored, provided it remains constant across each shock; a constant mass correction factor k_m , also does not enter, but the ion pressure correction k_p is needed to adjust the pressure anisotropies α and α_1 .

Comparison of the left side and the first term on the right side of (10) is shown in Figures 7h and 7i. They do indeed show a reasonably good overall fit, albeit with more substantial local deviations, in particular, for the downstream point of Shock 2, where $(1 - \alpha)$ has turned negative. Elsewhere, the deviations between green and black curves in Figures 7h and 7i could perhaps be an indication of the presence of viscous stresses. But the largest deviations are not where the largest velocity shear occurs, casting doubt on such an interpretation.

The large discrepancy, seen at the RD location (16:59:15 UT) in Figure 7g, is absent in Figure 7i. This behavior indicates that the Hall term, present in Ohm's law but not in the tangential stress balance, is the likely agent responsible for the discrepancy.

If viscous effects are negligible, the y and z component equations above can be rearranged and combined to form a different modification of the tangential part (but not the normal part) of the Walén relation, namely,

$$V'_{y,z} = V_{Ay,z}^* \sqrt{\rho(1-\alpha)/\rho_1(1-\alpha_1)} \quad (11)$$

With little or no resistive and viscous effects, the dissipation would have come about in a different way. That pressure anisotropy plays an important role is evident already from Figure 2g, in which it is seen that both shocks act to isotropize the plasma temperatures. In Shock 1 this occurs mostly by increasing T_{\perp} , in Shock 2 mostly by increasing T_{\parallel} .

In the absence of resistive, Hall, and viscous effects, equations (6) and (11) can be combined to yield

$$\rho(1-\alpha) = \rho_1(1-\alpha_1) \quad (12)$$

which would make such a switch-off shock indistinguishable from a dissipation-free rotational discontinuity, at least on the basis of whether or not equation (12) holds. Note that in calculating the product $\rho(1-\alpha)$, the ion pressure correction factor k_p must be included in α and the mass correction factor k_m in ρ . In Figure 7a, these corrections have been incorporated in the product, which is shown as the green curve. It is seen that the product exhibits large variations, caused by fluctuating, and probably not meaningful values of $(1-\alpha)$ in the center part of the event (see Figure 7b). At least in part, these fluctuations may be the result of active fire hose instability, which occurs for $\alpha > 1$. Within each shock, the behavior is more orderly but cannot be characterized as having a constant value of the product $\rho(1-\alpha)$. Our suspicion is that this product may in reality have been nonconstant in most of the events that have been identified in the past as magnetopause RDs. Even when the actually measured ion composition is included in the mass density, the product does not become constant, as recently demonstrated by *Blagau et al.* [2015]. For our event, these results pose an unresolved dilemma: On the one hand, we find no convincing evidence of the combined resistivity/Hall terms in Ohm's law or of viscous stresses in the tangential momentum law, which implies that the product $\rho(1-\alpha)$ should be constant, or at least approximately constant. On the other hand, we evaluate this product from the measurements (either without or with the ion pressure correction factor k_p) and find it to be far from constant.

5. Summary and Discussion

We have presented qualitative and quantitative analysis of an outbound magnetopause crossing of the dayside, low-latitude, magnetopause by the spacecraft THEMIS D during ongoing reconnection. The event exhibits high magnetic shear (152°) across the magnetopause with a southward directed high-speed plasma jet embedded in it. The jet direction and the sunward direction of the magnetic field component B_x normal to the magnetopause both indicate that the crossing occurred southward of a reconnection site. The Walén test (see Figure 4) illustrates that the flow is approximately field aligned in the deHoffmann-Teller (HT) frame but that the correlation between flow and field reverses sign, from positive on the magnetosphere side to negative on the magnetosheath side. Together with this reversal, the positive (sunward) B_x implies that there is inflow into the exhaust jet from both the magnetosheath and the magnetosphere side. In the HT frame, this two-sided inflow can also be seen directly in the velocity data (Figures 4f and 7e) as a reversal of the normal velocity component, $V'_x = V_x - V_{HTx}$, from sunward (positive) on the magnetospheric side of the event to earthward (negative) on the magnetosheath side.

The magnetic field components tangential to the magnetopause are very nearly switched off in the center of the event, leading to the conclusion that, as predicted by *Petschek* [1964], the exhaust jet is created by, and wedged between, two switch-off shocks, Shock 1 on the magnetospheric side and Shock 2 on the magnetosheath side. Basic features supporting this interpretation include theoretically predictable, enhanced, values of density, pressure, ion and electron temperatures, and entropy, in the exhaust jet. The large jumps of these thermodynamic quantities across Shock 1 and the much smaller jumps across Shock 2 is accounted for by the much lower plasma beta value in the magnetosphere (see section 3). But as discussed below, there are also observational features and limitations that complicate the picture.

Examination of the spacecraft potential (see Appendix A) revealed the presence, on the magnetospheric side, of a large population of ions with energies below the range of the plasma instrument ESA. The plasma composition is not measured but, from the Alfvénic nature of the flow, as seen in the HT frame immediately upstream of a switch-off shock, we have been able to approximately estimate the effective ion masses in the two shocks (see section 3.2). For Shock 1, the result was 2.39 amu with a wide range of uncertainty (1.41 to 2.49 amu) associated with the range of field-aligned flow speeds of the ions that fall below the ESA energy threshold. For Shock 2, in which one may presume that essentially all ions were recorded by ESA, the result was 1.09 amu corresponding to the presence of some 3% He⁺⁺. For both shocks there is additional uncertainty associated with possible errors in the HT frame velocity. Nevertheless, the results indicate that the mass flux into the exhaust jet from the magnetospheric side was in all likelihood larger than from the magnetosheath side, which can help account for the unusual configuration of two back-to-back switch-off shocks seen in this magnetopause event.

The average, earthward directed, magnetopause motion was found to be 14.1 km/s with a resulting width of ≈ 1227 km = $12.3\lambda_i$ for Shock 1 and ≈ 338 km = $6.1\lambda_i$ for Shock 2. Note that the duration used for Shock 1 includes a preshock interval of ≈ 300 km = $3.0\lambda_i$, in which a pronounced number density minimum occurs and in which a rotational discontinuity (RD) of width ≈ 140 km = $1.4\lambda_i$ is imbedded. The RD is an Alfvénic structure. It is located immediately upstream of Shock 1 because the latter is nearly at the switch-off limit so that its upstream state is also Alfvénic. In other words, the RD and the shock both propagate at the Alfvén speed based on the normal field component and therefore have zero wedge angle between them. There are indications in the time series of the magnetic field that there may be some small scale back-and-forth motion of the magnetopause so that individual structures may have had widths that deviate substantially from the above values. However, at least portions of the event has widths of only a few λ_i so that some effects of Hall physics should be visible. There is also evidence that a sharp local deformation (bend) of the structure was encountered between the two shocks.

The event does show indications both of Hall current loops manifested as out-of-plane magnetic fields, B_y , and strong bipolar electric fields E_x (in the spacecraft frame) pointing toward the middle of the event. But these Hall parts of the configuration are very asymmetric, with most of the Hall structure being located in the combined RD and Shock 1, i.e., on the magnetospheric side. There is also some weak evidence of Hall current loops associated with Shock 2.

The separatrix locations were not found in the observations but their locations, predicted from magnetic flux conservation, are substantially upstream of the shocks and of the RD structures at their upstream edges. The implication is that the observed density minimum, immediately preceding Shock 1, was not colocated with the separatrix on the magnetospheric side.

The pressure anisotropy factor α is weak in the magnetosphere but substantial and negative in the magnetosheath. In parts of the exhaust jet, one has $\alpha > 1$, which means that the fire hose instability should be active there.

There was little time delay between the downstream ends of the two shocks, indicating that they were still too close to the reconnection site to have been able to establish their final widths. In addition to the firehouse instability, the situation in the center of the exhaust jet may be further complicated by the fact that, according to resistive-dispersive theory [Hau and Sonnerup, 1990, 1992], a slow shock in our parameter regime is expected to have a standing, circularly polarized, wave train at its downstream end. In our event, the shocks may not be fully formed but there is perhaps some evidence for incipient, overlapping, wave trains in the partial ring formed by the hodogram trace around the origin of the high-resolution tangential hodogram.

We have shown that maintaining the balance of stresses in the direction normal to Shock 1 requires a multiplicative correction factor $k_p = 1.27$ for the ion pressures (see Table 3). This correction may be related to the presence of heavier ion species.

The interior structure of the shocks was investigated by use of Ohm's law and the tangential momentum equation. The results show no convincing signatures of the presence of ordinary resistivity and viscosity. The only possible indications of such effects were not found where expected, namely, where the electric current density and/or the velocity shear are largest. And the Hall electric fields themselves do not cause dissipation. It appears likely that dissipation in the shocks themselves comes mainly from irreversible transfer between the parallel and the perpendicular energy reservoirs.

Particle-in-cell simulations of the reconnection of antiparallel fields, and associated theoretical analysis [Liu *et al.*, 2012], have shown the formation of a plateau in the anisotropy factor α at the level $\alpha = 0.75$ in each of the two shocks bounding the plasma exhaust. Between these plateaus, the simulations show a region of $\alpha > 1$, indicating the presence of the fire hose instability. The (uncorrected) α values shown in Figure 4d, do indeed show some evidence for such plateaus, at least for Shock 1 with its much longer duration. And in the center of the exhaust region, the observed α values do indeed fluctuate between large positive and large negative values. We conclude that there is at least qualitative agreement between some of the simulation results and the observed behavior.

There is clear evidence in the measured plasma velocity components tangential to the magnetopause (see Table 1) on the two sides of the magnetopause that the frozen field condition is violated. Presumably this is the result of nonzero normal electric fields within the shocks and exhaust. This effect can lead to slippage of the various plasma layers of the event relative to each other and relative to the magnetic field, the result being that the jumps in the tangential velocity components across each shock may deviate from being Alfvénic. In our event, the jumps in the z component are indeed somewhat sub-Alfvénic, provided our nominal effective ion masses are correct.

The magnetopause structure during ongoing reconnection examined in this paper is unusual in that it involved large amounts of heavy ions on its magnetospheric side. Combined with the large magnetic shear angle, the result was a near switch-off of the tangential magnetic field, i.e., a deep field minimum in the middle of the layer. The event can therefore not be described by standard component reconnection models. Numerical simulations that mimic the conditions in our event could help shed light on the detailed physics.

Cursory inspection of magnetopause reconnection events in which the configuration remains strongly asymmetric indicates that they usually show substantial field magnitude minima and also somewhat sub-Alfvénic flow. For these two reasons, one can surmise that most such events must contain elements of slow-mode shocks, in addition to the RDs needed to accommodate the magnetic shear angle. They may also exhibit the slippage of plasma relative to magnetic field mentioned above.

Appendix A: Cold Plasma

As shown by the ion spectrogram (Figure A1a), there is “cold” (up to tens of eV) plasma within the magnetosphere side of the exhaust. Inspection of the distribution functions indicates that this cold plasma extends until about 17:00:20 UT. Figure A2 shows such a distribution function, measured near 16:59:23 UT. The spacecraft electric potential makes clear, however, that on the magnetospheric side there is additional plasma that is initially not detected by the ESA instrument. Ions need to have energies above ≈ 10 eV to be measured, given the ion instrument’s low-energy threshold of ≈ 5 eV and the spacecraft potential of $\approx +5$ eV at this time. Electrons gain ≈ 5 eV from the potential, but the electron instrument’s low-energy threshold is ≈ 7 eV at the time. Thus, electrons are not recorded if their energy is less than ≈ 2 eV.

Figure A1b shows the ESA-measured densities (black for ions, red for electrons), which are very low (generally less than 1 1/cm^3) in the magnetosphere. Superimposed (in green) is the density inferred from the spacecraft potential measurements by the EFI instrument [Bonnell *et al.*, 2008]. It shows a density near 10 1/cm^3 in the magnetosphere but agrees quite well with the ESA-based densities in the exhaust, because the cold ions have been accelerated as they enter the exhaust so that they are now within the ESA energy range. There is also an early density peak near 16:58:20 UT, presumably caused by a brief encounter with the magnetopause. In this brief peak, the cold ions have been accelerated to a sufficient extent so that the ESA ion density agrees with the potential-derived density, but the electron density remains very low, indicating that their energy remained less than ≈ 2 eV.

The cold plasma, undetected by the ESA instrument, must also affect the temperatures. Assuming that the cold plasma does not contribute to the plasma pressure, the effective temperatures can be calculated by dividing the ion and electron pressures measured by the ESA instrument by the composite density (green curve in Figure A1b). Figure A1c shows, as the black and red traces, respectively, the ion and electron temperatures ($T = (T_{\parallel} + 2 T_{\perp})/3$), obtained by dividing the ESA-measured ion and electron pressures by the respective ESA densities, and as the blue and green traces the temperatures obtained by dividing the same pressures by the composite density. As the figure shows, the temperatures based on the composite density now rise rather than drop when entering the exhaust from the magnetosphere side.

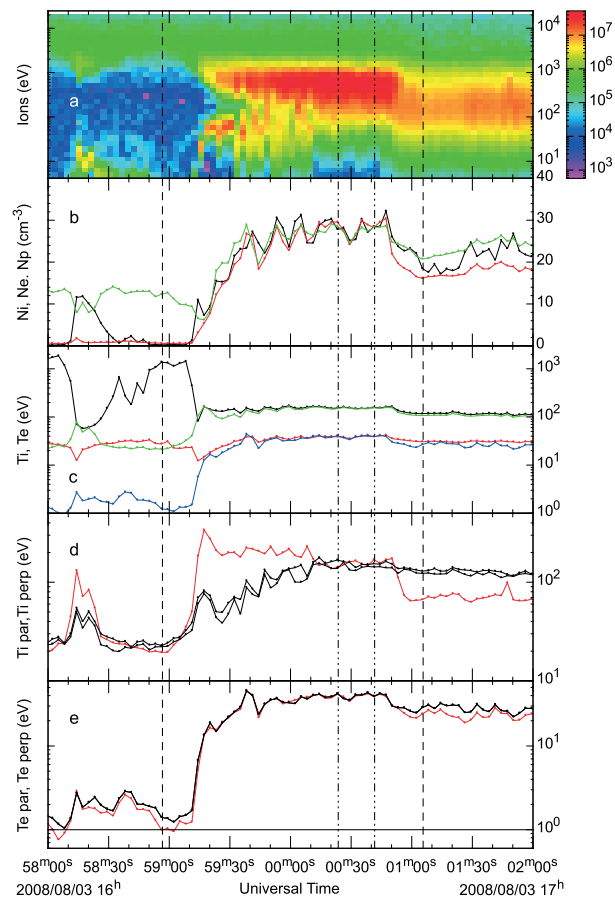


Figure A1. Densities and temperatures including the cold plasma. (a) Ion energy-time spectrogram (color bar units are $\text{eV}/\text{cm}^2 \text{ s}$). (b) Ion (black) and electron (red) number densities (N_i , N_e) as measured by the ESA instrument, plus the density, N_p , inferred from the spacecraft potential (green). A composite density (referred to simply as N in all time series figures and equations in the paper) has been constructed, consisting of the potential-based density up to 16:59:35 UT (green trace), and the ESA-based ion density (black trace) thereafter. (c) Ion (black) and electron (red) temperatures (in eV), obtained by dividing the ESA-measured pressures by the densities N_i and N_e , respectively, plus the ion (blue) and electron (green) temperatures obtained by dividing the ESA-measured pressures by the composite density. (d) The ion parallel (red) and the two perpendicular (black) temperatures, also obtained by dividing the pressures by the composite density. (e) The same for electrons.

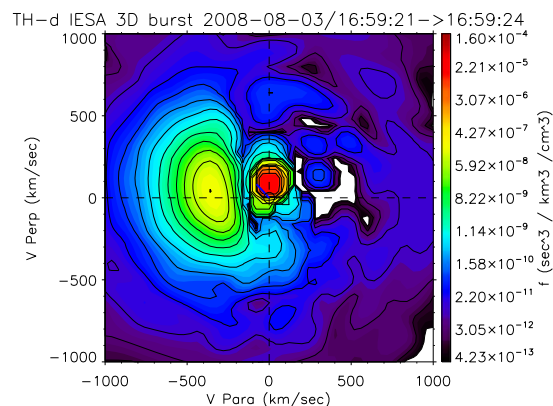


Figure A2. Two-dimensional ion distribution function in the \mathbf{V}_{\parallel} and \mathbf{V}_{\perp} plane. It was sampled in a single 3 s spin period. The crescent-shaped component on the left represents the accelerated magnetosheath distribution, while the red component near the origin represents the cold ions from the magnetosphere. Phase space densities are color coded as shown on the right.

It is interesting to note that, using the magnetospheric temperature corrected for the presence of the cold plasma, the (effective) inflow temperature is lowered, while the exhaust temperature stays the same, leading to an increased ΔT_i , the resulting value being much closer to the prediction from the empirical formula developed by Phan *et al.* [2014].

Figures A1c and A1d show the three diagonal elements of the ion temperature tensor, obtained by dividing the magnetic field-oriented pressure tensor by the composite electron density. The red trace represents T_{\parallel} , and the two black traces represent T_{\perp} as the maximum and minimum values in the plane perpendicular to \mathbf{B} . The ion parallel temperature increases strongly when entering the exhaust from the magnetosphere side, an effect caused by the relative motion of the cold and hot ion populations. The perpendicular temperature increases more slowly, until isotropy is reached. Entering the exhaust from the magnetosheath side, the parallel temperature rises sharply too, until it agrees with the perpendicular temperature. The electron temperatures in Figure A1e, obtained the same way, indicate near isotropy. As it is shown, the two black traces in the Figures A1d and A1e are nearly equal throughout, meaning that the distributions are essentially gyrotropic.

While the assumption that the cold ions have no intrinsic pressure seems reasonable, any relative velocity between the cold and hot ions, such as shown in Figure A2, for times when the cold ions have become visible, will introduce a contribution to p_{\parallel} . Thus, the parallel temperatures obtained by dividing the pressures by the composite density will have too low values. This is a likely explanation for the pressure correction factor, $k_p = 1.27$, needed in Shock 1.

The cold plasma should also affect the bulk velocity. The large discrepancy between the z components of the plasma velocity \mathbf{V} and the Alfvén velocity (see Figure 4h) at the beginning of the event is probably in part related to this fact. First, the density around 10 1/cm^3 is dominated by the cold plasma inferred from the spacecraft potential, while the density recorded by the ESA instrument is only around 0.2 1/cm^3 . Thus, the bulk velocity measured by ESA is probably not representative of the plasma as a whole. This is confirmed by a comparison (not shown) of the components of V_{\perp} , as measured by ESA, with the components of $(\mathbf{E} \times \mathbf{B})/B^2$ (with \mathbf{E} measured by EFI), which shows that there is agreement only where there is sufficient density. We have formally incorporated this effect via the velocity correction factor with an upper limit $k_v < 1.30$. However, the second, and dominant, reason for the discrepancy is that \mathbf{V}_A , calculated under the assumption that all ions are protons (as was the case in Figure 4), would be overestimated, if heavier ions are present. There is persuasive evidence for the presence of such ions with effective ion mass ratio in the range $1.41 < k_m < 2.49$, as discussed in section 3.2.

Acknowledgments

The research reported here is part of an International Team effort supported by the International Space Science Institute (ISSI), Bern, Switzerland. We thank the team members for valuable comments on our work. And we particularly thank F. Mozer for providing number densities derived from spacecraft charging. We thank the THEMIS team for providing well-calibrated plasma and field data. Data source: THEMIS Data Center at themis.ssl.berkeley.edu. The individual research efforts were sponsored by NASA under grant NNX12AH43G to University of Colorado Boulder (B.S. and S.E) and by grant NNX08AO83G to University of California, Berkeley (T.P.). S.H. was supported by the Norwegian Research Council under grant BCSS 223252. G.P. has support in the form of guest status at MPE Garching. The data analysis has made use of the QSAS science analysis system, provided by Imperial College, London, and available at www.sp.ph.ic.ac.uk/csc-web/QSAS/. We dedicate the paper to the memory of H.E. Petschek, whose pioneering work on the reconnection problem continues to inspire and inform.

References

- Auster, H. U., *et al.* (2008), The THEMIS fluxgate magnetometer, *Space Sci. Rev.*, *141*, 235–264, doi:10.1007/s11214-008-9365-9.
- Birn, J., *et al.* (2001), Geospace Environmental Modeling (GEM) magnetic reconnection challenge, *J. Geophys. Res.*, *106*, 3715–3720, doi:10.1029/1999JA900449.
- Blagau, A., G. Paschmann, B. Klecker, and O. Marghitsu (2015), Experimental test of the $p(1-\alpha)$ evolution for rotational discontinuities: Cluster magnetopause observations, *Ann. Geophys.*, *33*, 79–91, doi:10.5194/angeo-33-79-2015.
- Bonnell, J. W., F. S. Mozer, G. T. Delory, A. J. Hull, R. E. Ergun, C. M. Cully, V. Angelopoulos, and P. R. Harvey (2008), The Electric Field Instrument (EFI) for THEMIS, *Space Sci. Rev.*, *141*, 303–341, doi:10.1007/s11214-008-9469-2.
- Borovsky, J. E., M. H. Denton, R. E. Denton, V. K. Jordanova, and J. Krall (2013), Estimating the effects of ionospheric plasma on solar wind/magnetosphere coupling via mass loading of dayside reconnection: Ion-plasma-sheath oxygen, plasmaspheric drainage plumes, and the plasma cloak, *J. Geophys. Res. Atmos.*, *118*, 5695–5719, doi:10.1002/jgra.50527.
- Eastwood, J. P., M. A. Shay, T. D. Phan, and M. Øieroset (2010), Asymmetry of the ion diffusion region Hall electric and magnetic fields during guide field reconnection: Observations and comparison with simulations, *Phys. Rev. Lett.*, *104*(20), 205001, doi:10.1103/PhysRevLett.104.205001.
- Eriksson, S., M. Øieroset, D. N. Baker, C. Moukik, A. Vaivads, M. W. Dunlop, H. Rème, R. E. Ergun, and A. Balogh (2004), Walén and slow-mode shock analyses in the near-Earth magnetotail in connection with a substorm onset on 27 August 2001, *J. Geophys. Res.*, *109*, A10212, doi:10.1029/2004JA010534.
- Feldman, W. C., D. N. Baker, S. J. Bame, J. Birn, J. T. Gosling, E. W. Hones Jr., and S. J. Schwartz (1985), Slow-mode shocks: A semipermanent feature of the distant geomagnetic tail, *J. Geophys. Res.*, *90*, 233–240, doi:10.1029/JA090iA01p00233.
- Gosling, J. T., R. M. Skoug, D. J. McComas, and C. W. Smith (2005), Direct evidence for magnetic reconnection in the solar wind near 1 AU, *J. Geophys. Res.*, *110*, A01107, doi:10.1029/2004JA010809.
- Hau, L.-N., and B. U. Ö. Sonnerup (1990), The structure of resistive-dispersive intermediate shocks, *J. Geophys. Res.*, *95*, 18,791–18,808, doi:10.1029/JA095iA11p18791.
- Hau, L.-N., and B. U. Ö. Sonnerup (1992), The thickness of resistive-dispersive shocks, *J. Geophys. Res.*, *97*, 8269–8275, doi:10.1029/92JA00138.
- Kantrowitz, A., and H. E. Petschek (1966), MHD characteristics and shock waves, in *Plasma Physics in Theory and Application*, edited by W. B. Kunkel, chap. 6, pp. 147–206, McGraw-Hill, New York.

- Karimabadi, H., J. D. Huba, D. Krauss-Varban, and N. Omid (2004), On the generation and structure of the quadrupole magnetic field in the reconnection process: Comparative simulation study, *Geophys. Res. Lett.*, *31*, L07806, doi:10.1029/2004GL019553.
- Khotyaintsev, Y. V., A. Vaivads, A. Retinò, M. André, C. J. Owen, and H. Nilsson (2006), Formation of inner structure of a reconnection separatrix region, *Phys. Rev. Lett.*, *97*(20), 205003, doi:10.1103/PhysRevLett.97.205003.
- Khrabrov, A. V., and B. U. Ö. Sonnerup (1998), DeHoffmann-Teller analysis, in *Analysis Methods for Multi-Spacecraft Data, ISSI SR-001*, edited by G. Paschmann and P. W. Daly, pp. 221–248, ESA Publ. Div., Noordwijk, Netherlands.
- Levy, R. H., H. E. Petschek, and G. L. Siscoe (1964), Aerodynamic aspects of the magnetospheric flow, *AIAA J.*, *2*, 2065–2076.
- Lin, Y., and L. C. Lee (1993), Structure of the dayside reconnection layer in resistive MHD and hybrid models, *J. Geophys. Res.*, *98*, 3919–3934, doi:10.1029/92JA02363.
- Liu, Y.-H., J. F. Drake, and M. Swisdak (2012), The structure of the magnetic reconnection exhaust boundary, *Phys. Plasmas*, *19*(2), 022110, doi:10.1063/1.3685755.
- Malakit, K., M. A. Shay, P. A. Cassak, and C. Bard (2010), Scaling of asymmetric magnetic reconnection: Kinetic particle-in-cell simulations, *J. Geophys. Res.*, *115*, A10223, doi:10.1029/2010JA015452.
- McFadden, J. P., C. W. Carlson, D. Larson, M. Ludlam, R. Abiad, B. Elliott, P. Turin, M. Marckwordt, and V. Angelopoulos (2008), The THEMIS ESA plasma instrument and in-flight calibration, *Space Sci. Rev.*, *141*, 277–302, doi:10.1007/s11214-008-9440-2.
- Mozer, F. S., S. D. Bale, and T. D. Phan (2002), Evidence of diffusion regions at a subsolar magnetopause crossing, *Phys. Rev. Lett.*, *89*(1), 015002, doi:10.1103/PhysRevLett.89.015002.
- Nagai, T., I. Shinohara, M. Fujimoto, M. Hoshino, Y. Saito, S. Machida, and T. Mukai (2001), Geotail observations of the Hall current system: Evidence of magnetic reconnection in the magnetotail, *J. Geophys. Res.*, *106*, 25,929–25,950, doi:10.1029/2001JA900038.
- Øieroset, M., T. D. Phan, M. Fujimoto, R. P. Lin, and R. P. Lepping (2001), In situ detection of collisionless reconnection in the Earth's magnetotail, *Nature*, *412*, 414–417, doi:10.1038/35086520.
- Øieroset, M., T. D. Phan, J. T. Gosling, M. Fujimoto, and V. Angelopoulos (2015), Electron and ion edges and the associated topology of the reconnecting magnetopause, *J. Geophys. Res. Space Physics*, *120*, 9294–9306, doi:10.1002/2015JA021580.
- Paschmann, G., and B. U. Ö. Sonnerup (2008), Proper frame determination and Walén test, in *Multi-Spacecraft Analysis Methods Revisited, ISSI Sci. Rep. SR-008*, edited by G. Paschmann and P. W. Daly, chap. 7, pp. 65–74, ESA Commun., Noordwijk, Netherlands.
- Paschmann, G., I. Papamastorakis, W. Baumjohann, N. Sckopke, C. W. Carlson, B. U. Ö. Sonnerup, and H. Lühr (1986), The magnetopause for large magnetic shear—AMPTE/IRM observations, *J. Geophys. Res.*, *91*, 11,099–11,115, doi:10.1029/JA091iA10p11099.
- Paschmann, G., M. Øieroset, and T. Phan (2013), In-situ observations of reconnection in space, *Space Sci. Rev.*, *178*, 385–417, doi:10.1007/s11214-012-9957-2.
- Petschek, H. E. (1964), Magnetic field annihilation, in *Proceedings of the AAS-NASA Symposium on the Physics of Solar Flares*, edited by W. N. Hess, pp. 425–439, NASA, Washington, D. C.
- Petschek, H. E., and R. M. Thorne (1967), The existence of intermediate waves in neutral sheets, *Astrophys. J.*, *147*, 1157, doi:10.1086/149105.
- Phan, T. D., J. F. Drake, M. A. Shay, F. S. Mozer, and J. P. Eastwood (2007), Evidence for an elongated (>60 ion skin depths) electron diffusion region during fast magnetic reconnection, *Phys. Rev. Lett.*, *99*(25), 255002, doi:10.1103/PhysRevLett.99.255002.
- Phan, T. D., M. A. Shay, J. T. Gosling, M. Fujimoto, J. F. Drake, G. Paschmann, M. Øieroset, J. P. Eastwood, and V. Angelopoulos (2013), Electron bulk heating in magnetic reconnection at Earth's magnetopause: Dependence on the inflow Alfvén speed and magnetic shear, *Geophys. Res. Lett.*, *40*, 4475–4480, doi:10.1002/grl.50917.
- Phan, T. D., J. F. Drake, M. A. Shay, J. T. Gosling, G. Paschmann, J. P. Eastwood, M. Øieroset, M. Fujimoto, and V. Angelopoulos (2014), Ion bulk heating in magnetic reconnection exhausts at Earth's magnetopause: Dependence on the inflow Alfvén speed and magnetic shear angle, *Geophys. Res. Lett.*, *41*, 7002–7010, doi:10.1002/2014GL061547.
- Pritchett, P. L., and F. S. Mozer (2009), Asymmetric magnetic reconnection in the presence of a guide field, *J. Geophys. Res.*, *114*, A11210, doi:10.1029/2009JA014343.
- Sharma, A. S., et al. (2008), Transient and localized processes in the magnetotail: A review, *Ann. Geophys.*, *26*, 955–1006, doi:10.5194/angeo-26-955-2008.
- Shay, M. A., J. F. Drake, B. N. Rogers, and R. E. Denton (2001), Alfvénic collisionless magnetic reconnection and the Hall term, *J. Geophys. Res.*, *106*, 3759–3772, doi:10.1029/1999JA001007.
- Sonnerup, B. U. Ö. (1979), Magnetic field reconnection, in *Solar System Plasma Processes*, vol. 3, edited by L. J. Lanzerotti, C. F. Kennel, and E. N. Parker, pp. 45–108, North-Holland, Washington, D. C.
- Sonnerup, B. U. Ö., and M. Scheible (1998), Minimum and maximum variance analysis, in *Analysis Methods for Multi-Spacecraft Data, ISSI Sci. Rep. SR-001*, edited by G. Paschmann and P. W. Daly, chap. 8, pp. 185–220, ESA Publ. Div., Noordwijk, Netherlands.
- Sonnerup, B. U. Ö., G. Paschmann, and T.-D. Phan (1995), Fluid aspects of reconnection at the magnetopause: In situ observations, in *Physics of the Magnetopause, Geophys. Monogr. Ser.*, vol. 90, edited by P. Song, B. U. Ö. Sonnerup, and M. F. Thomsen, pp. 167–180, AGU, Washington, D. C.
- Teh, W.-L., R. Nakamura, B. U. Ö. Sonnerup, J. P. Eastwood, M. Volwerk, A. N. Fazakerley, and W. Baumjohann (2011), Evidence of the origin of the Hall magnetic field for reconnection: Hall MHD reconstruction results from Cluster observations, *J. Geophys. Res.*, *116*, A11218, doi:10.1029/2011JA016991.
- Toledo-Redondo, S., A. Vaivads, M. André, and Y. V. Khotyaintsev (2015), Modification of the Hall physics in magnetic reconnection due to cold ions at the Earth's magnetopause, *Geophys. Res. Lett.*, *42*, 6146–6154, doi:10.1002/2015GL065129.